Available online at www.sciencedirect.com
ScienceDirect
Trans. Nonferrous Met. Soc. China 34(2024) 1136−1149
Transactions of Nonferrous Metals Society of China
www.tnmsc.cn

Strengthening behavior and model of ultra-high strength Ti−15Mo−2.7Nb−3Al−0.2Si titanium alloy

Xiao-hui SHI[1], Qi ZHANG[1], Zhen JING[1], Zhi-yuan FAN[1], Jiang-lin LIU[2], Jun-wei QIAO[1]

1. College of Materials Science and Engineering, Taiyuan University of Technology, Taiyuan 030024, China;
2. College of Mechanical and Vehicle Engineering, Taiyuan University of Technology, Taiyuan 030024, China

Received 27 September 2022; accepted 11 April 2023

Abstract: The microstructure evolution and strengthening behavior of the ultra-high strength Ti−15Mo−2.7Nb−3Al−0.2Si titanium alloy were studied utilizing XRD, OM, SEM, and TEM analyses. The results show that the dislocation-strengthening and precipitation-strengthening effects could mostly affect the yield strength of this alloy. The highest yield strength of 1518 MPa was obtained under a combined process of cold rolling + recrystallization + cold rolling + duplex aging. This trend is mainly due to the high density of remaining dislocations, as well as dense and thin secondary α phases in microstructures. A theoretical composite-strengthening model was built, and the prediction error is within 16.6%. Furthermore, it is found that increasing the content of the secondary α phase can continuously strengthen the intragrain zone. This feature causes the intergranular fracture to appear and gradually dominate the fracture surface.

Key words: strengthening model; ultra-high strength; strengthening behavior; titanium alloy; Ti−15Mo−2.7Nb−3Al−0.2Si

1 Introduction

Nowadays, the rapid development of a new generation of aircrafts in the direction of high speed, large size, complex structure, and improved fuel efficiency has given rise to higher requirements for the strength, toughness, and other properties of aerospace materials [1−4]. Titanium alloys are widely used in the manufacture of key components in aircrafts because of the advantages of low density, high strength, good toughness, etc. Among them, the pursuit of high strength is the key to its application. At present, the development of ultra-high strength ($\sigma_b \geq 1250$ MPa) titanium alloys is very active [5−7].

Metastable β type titanium alloys contain β stable elements with Mo equivalent in the range of 13.8−25 wt.%. Being air-cooled or water-quenched after the solution treatment in the β-phase region, followed by the aging treatment, a very high strength can be achieved. The Ti−15Mo−2.7Nb−3Al−0.2Si alloy is a typical metastable β-type titanium alloy and could achieve an ultra-high strength. It has been widely used in the manufacture of fasteners in the aerospace industry [8−10]. To expand the scope of its aviation applications and promote the development and application of high-reliability aviation aircraft, it is of great significance to realize continuous improvement in its strength. Since the birth of the Ti−15Mo−2.7Nb−3Al−0.2Si alloy, many scholars have tried various deformation and heat treatment methods to control its microstructure and obtain ultra-high strength. XU et al [11] achieved the ultimate tensile strength of 1437 MPa of the Ti−15Mo−2.7Nb−3Al−0.2Si alloy through duplex aging. By combining the solution treatment in the β single-

Corresponding author: Xiao-hui SHI, Tel: +86-351-6010533, E-mail: sxhtough@126.com
DOI: 10.1016/S1003-6326(23)66459-3

phase, followed by quenching, room-temperature cold deformation, recrystallization annealing, and aging treatment, IVASISHIN et al [12] obtained a tensile strength up to 1620 MPa. XU et al [13] found that after a cold-deformation and aging process, the tensile strength of the Ti−15Mo−2.7Nb−3Al−0.2Si alloy can exceed 1700 MPa.

The above research realized the continuous strength improvement of the Ti−15Mo−2.7Nb−3Al−0.2Si alloy through different processes. However, few reports have been found on the strength quantification of this alloy. The role of different strengthening mechanisms (intrinsic-strengthening, solid-solution-strengthening, grain-boundary-strengthening, dislocation-strengthening, and precipitation-strengthening) in the strength formation of this alloy is still unclear. This feature brings difficulty to the strength adjustment and could restrict the further improvement of its strength. To solve this problem, a theoretical composite-strengthening model should be built considering these five strengthening mechanisms. In the present work, several basic experiments were designed and conducted, and then the strengthening behavior and model of the Ti−15Mo−2.7Nb−3Al−0.2Si alloy were investigated.

2 Experimental

The as-received Ti−15Mo−2.7Nb−3Al−0.2Si alloy was supplied in the shape of bar with a diameter of around 50 mm. The β-transus temperature is approximately 800 °C. The chemical composition was tested according to the standard GB/T 4698—2011, and the result is listed in Table 1. To obtain a homogeneous initial microstructure of the bar, a solid-solution treatment (named SS for short) of 850 °C, 40 min was performed, followed by water quenching (WQ). The initial microstructure after the solid-solution treatment is shown in Fig. 1. The original β grains have an average grain size of 71.5 μm.

Table 1 Chemical composition of as-received Ti−15Mo−2.7Nb−3Al−0.2Si alloy (wt.%)

Al	Mo	Nb	Si	Fe
3.10	15.23	2.77	0.21	0.02
C	O	N	H	Ti
0.009	0.091	0.005	0.0017	Bal.

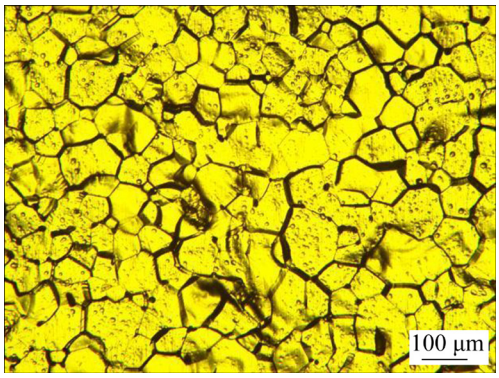

Fig. 1 Initial microstructure of Ti−15Mo−2.7Nb−3Al−0.2Si alloy after solid-solution treatment

The elongated samples with dimensions of 75 mm (length) × (15−20) mm (width) × 10/7/4 mm (three kinds of thickness) were sectioned by electrical discharge machining from the heat-treated billet. All of these samples were then cold rolled to 2 mm, which corresponds to reductions of 80% (named CR80%), 71% (named CR71%), and 50% (named CR50%), respectively. Three recrystallization annealing treatments, (920 °C, 5 min, WQ), (890 °C, 5 min, WQ), (815 °C, 5 min, WQ) were designed to achieve three different β-grain sizes of the Ti−15Mo−2.7Nb−3Al−0.2Si alloy. Subsequently, the single-stage aging plus cold rolling, duplex aging plus cold rolling, and cold rolling plus duplex aging treatments were performed. The specific processes and the corresponding process names were listed in Table 2.

The metallographic specimens were prepared under different processes by grinding, polishing, and corrosion. For specimens without the aging treatment, the corrodent is the mixture of HF, HNO_3, and H_2O with a volume ratio of 2:5:6. For specimens with the aging treatment, the volume ratio changes to 2:5:18. The microstructure morphologies were observed using a Leica optical microscope and a Phenom desktop scanning electron microscope. To obtain a more precise observation of the microstructure, we used a JEM−F200 transmission electron microscope. TEM foils were processed at a voltage of 20 V and a temperature of −35 °C using the MTP-1A automatic twinjet electropolisher. The XRD technique was used to carry out phase analysis and dislocation-density evaluation. The XRD device is of an Ultima IV type made by Rigaku Corporation. The scanning through the K_α radiation of the Cu target started

Table 2 Specific processes carried out in present work

Process	Process name	Specific process
Cold rolling	A	CR50%
	B	CR71%
	C	CR80%
Cold rolling+ Recrystallization	D	CR50%+ (920 °C, 5 min, WQ)
	E	CR71%+ (890 °C, 5 min, WQ)
	F	CR80%+ (815 °C, 5 min, WQ)
Cold rolling+ Recrystallization+ Aging+ Cold rolling	G	CR80%+ (815 °C, 5 min, WQ)+ (540 °C, 8 h, AC)+50%*
	H	CR80%+ (815 °C, 5 min, WQ)+ (350 °C, 2 h, AC)+ (540 °C, 8 h, AC)+50%*
Cold rolling+ Recrystallization+ Cold rolling+Aging	I	CR80%+(815 °C, 5 min, WQ)+50%*+ (350 °C, 2 h, AC)+ (540 °C, 8 h, AC)

* The rolling degree of 50% means that the thickness of the plate reduces from 2 to 1 mm

from 20° to 90° at a fixed scanning rate of 20 (°)/min. Tabular-shaped tensile specimens with a gauge length of 10 mm and a width of 3 mm were sectioned from the samples under different conditions. The Instron 5969 mechanical-testing machine was used, and the stroke rate was set to be 0.6 mm/min. Two specimens were applied under each process.

Obtaining the elastic parameters of the Ti−15Mo−2.7Nb−3Al−0.2Si alloy is essential to establish the yield strength model. An advanced non-destructive inspection technique called "ultrasonic echo analysis" was applied to detecting the elastic parameters of this alloy. Using the UMS−100 testing device, the ultrasonic wave with a frequency of 80 MHz was emitted through the probe and spread within the samples. Related echo signals were collected, and the valid part of them was selected by the professional identification of the engineer. Finally, the elastic parameters, including elastic modulus, shear modulus, and Poisson's ratio, were calculated and then output through the embedded program. Five cuboids of the Ti−15Mo−2.7Nb−3Al−0.2Si alloy (the solid-solution state, (830 °C, 30 min)) with section dimensions of around 3 mm × 3 mm were used. In the present work, the detected average values of elastic modulus, shear modulus, and Poisson's ratio are 76.9 GPa, 28.9 GPa, and 0.33, respectively. The shear-modulus value is similar to 27 GPa used by COURY et al [14].

3 Results and discussion

3.1 Yield strength

Figure 2(a) shows the original tensile curves of the Ti−15Mo−2.7Nb−3Al−0.2Si alloy after different processes. Due to the limit of the specimen size, the extensometer was not applied, and therefore, the initial elastic part of the tensile curves is not correct. To obtain accurate values of yield strength, the stiffness of the test machine was evaluated and then subtracted by the tensile curves in Fig. 2(a). The corrected engineering strain−stress curves after different processes are shown in Fig. 2(b). The yield strengths of this alloy after different processes were determined through the 0.2%-offset method and are listed in Table 3, which exhibit high repeatability.

Due to the coarse β grains in the micro-structure, as well as the absence of dislocation-strengthening and precipitation-strengthening effects, the average yield strength in the solid-solution state is only 740 MPa. Cold rolling introduced dislocations in the alloy, which increased the yield strength by approximately 200 MPa. It can be found that the yield strengths after Processes A−C show little variation. This trend means that the dislocation densities introduced by the three rolling degrees are similar. After the recrystallization annealing, the dislocation-strengthening effect was eliminated, and the grain-boundary-strengthening effect appeared. Figure 3 shows the grain sizes after Processes D, E, and F. The obvious result is that, by combining a higher rolling degree and a lower annealing temperature, the recrystallized grain size could be smaller. The average grain sizes after Processes D, E, and F, are 39, 24, and 14 μm, respectively. Due to the gradual increase in grain-boundary-strengthening effect, the yield strengths after Processes D, E, and F gradually increase from 816 to 829 MPa and finally to 844 MPa.

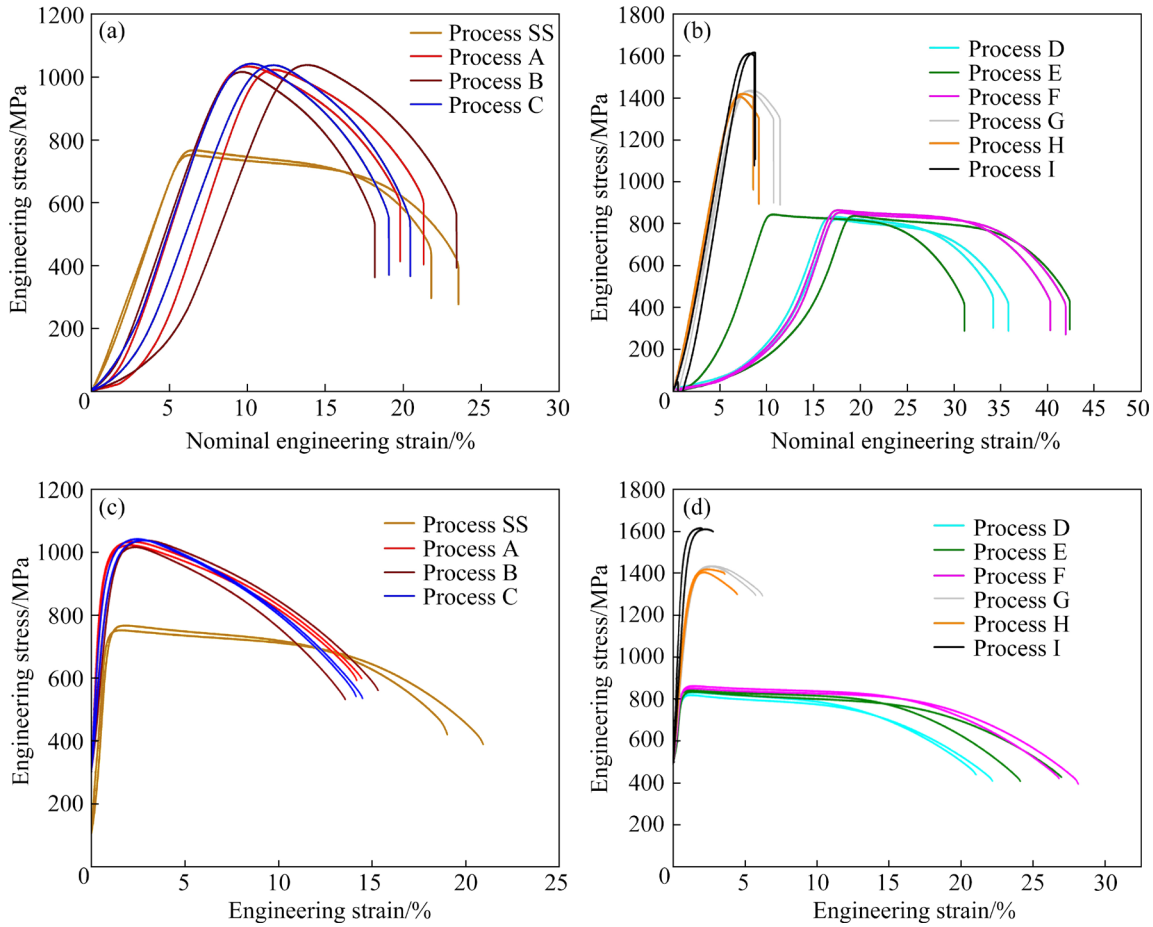

Fig. 2 Original tensile curves without extensometer (a, b) and corrected engineering strain−stress curves (c, d) of Ti−15Mo−2.7Nb−3Al−0.2Si alloy after different processes

Table 3 Yield strengths of Ti−15Mo−2.7Nb−3Al−0.2Si alloy after different processes

Process	Yield strength/MPa
SS	740±3.5
A	955±0.5
B	948±6
C	939±2.5
D	816±5
E	829±3.5
F	844±5.5
G	1314±2
H	1304±3
I	1518±2

Figure 4 shows the SEM images of the microstructures after Processes G and H. It can be easily seen that the high density of the needle-like tiny secondary α phase with different orientations is uniformly distributed inside β grains. Compared to the solid-solution state, the Ti−15Mo−2.7Nb−3Al−0.2Si alloy after Processes G and H, combines grain-boundary-strengthening, dislocation-strengthening, and precipitation-strengthening effects simultaneously, and therefore achieves high yield strengths, which are above 1300 MPa. The yield strengths after Processes G and H are almost the same, which indicates that the single-stage-aging treatment and the duplex-aging treatment generate similar precipitation-strengthening effects.

The highest yield strength was achieved after Process I. According to Table 3, the average yield strength after Process I can reach 1518 MPa. Compared to Processes G and H, Process I changes the sequence of aging treatment and cold rolling. However, this process leads to a large jump in yield strength of approximately 200 MPa. To explain this phenomenon, the differences in their microstructure features must be clarified. The TEM technique was used, considering that the tiny secondary α phase is

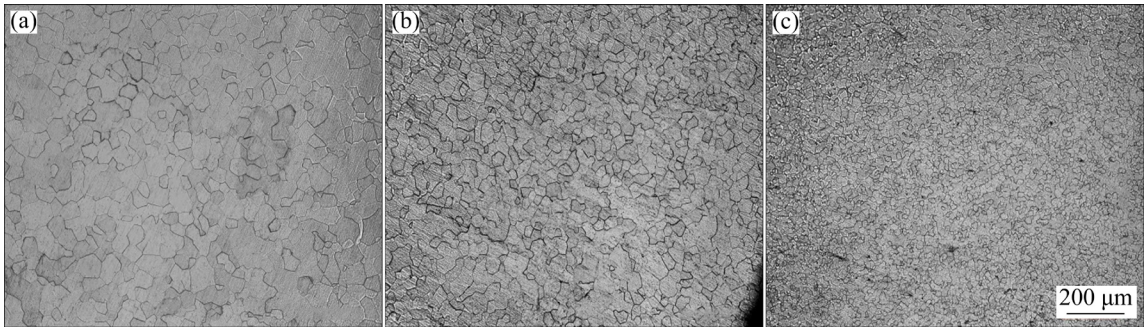

Fig. 3 Grain sizes after recrystallization annealing: (a) Process D; (b) Process E; (c) Process F

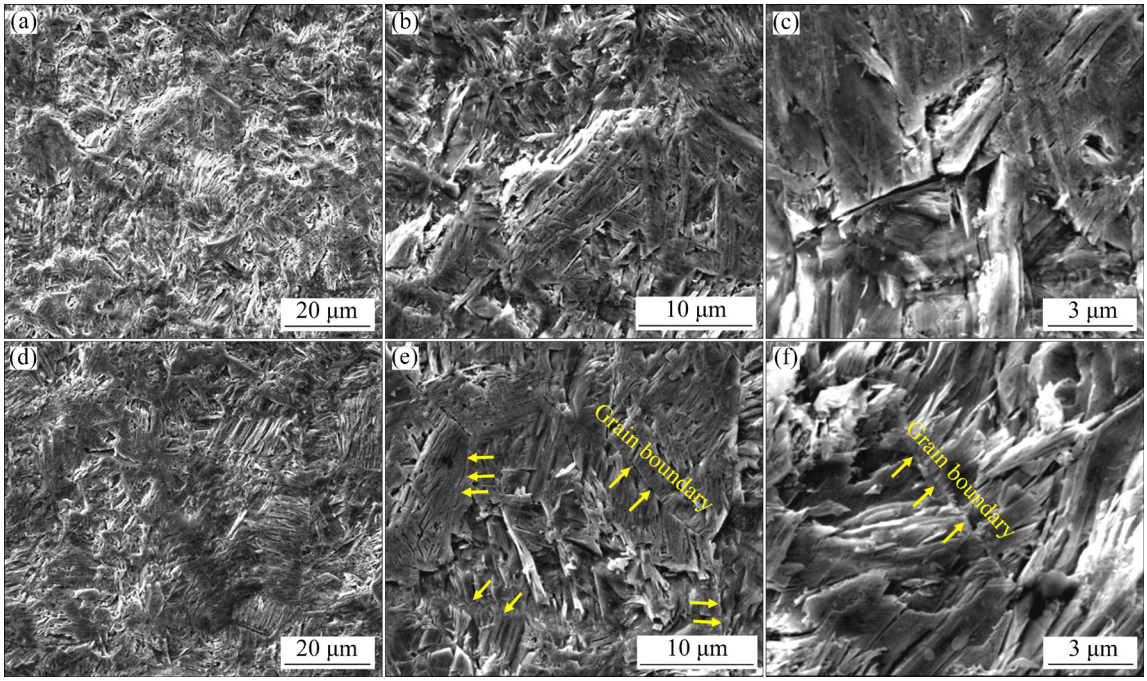

Fig. 4 SEM images of microstructures: (a−c) Process G; (d−f) Process H

difficult to distinguish. Figure 5 shows the TEM/SEM morphologies after Processes H and I. It can be found that the secondary α lamellae in microstructure after Process I (Figs. 5(e, f)) are much denser and smaller than those in microstructure after Process H (Fig. 5(b)). It can be explained in this way: After the cold rolling was exerted on the recrystallized specimens, a high density of dislocations was introduced into the microstructure. During the subsequent aging treatment, pre-existing dislocations became preferential-precipitation sites of the secondary α phase [15,16]. As a result, a much denser and thinner secondary α phase in the microstructure can be obtained. According to research [17], densely distributed precipitates with small spacing lead to high-frequent interactions between dislocations and precipitates. This trend could cause strong pinning effects. Furthermore, it was reported [18] that fine precipitates exhibit a stronger strengthening effect than bulky precipitates. In summary, it is speculated that the compact secondary α phase could result in a good precipitation-strengthening effect. In addition, there may be a considerable density of remaining dislocations in the microstructure after aging. Therefore, the dislocation-strengthening effect could be kept. This is possibly why the Ti−15Mo−2.7Nb−3Al−0.2Si alloy after Process I shows the highest yield strength.

LUO et al [19,20] conducted much valuable research on the microstructure evolution and mechanical properties of beta-type titanium alloys containing Si. They found that the introduction of Si can promote the formation of silicides, such as

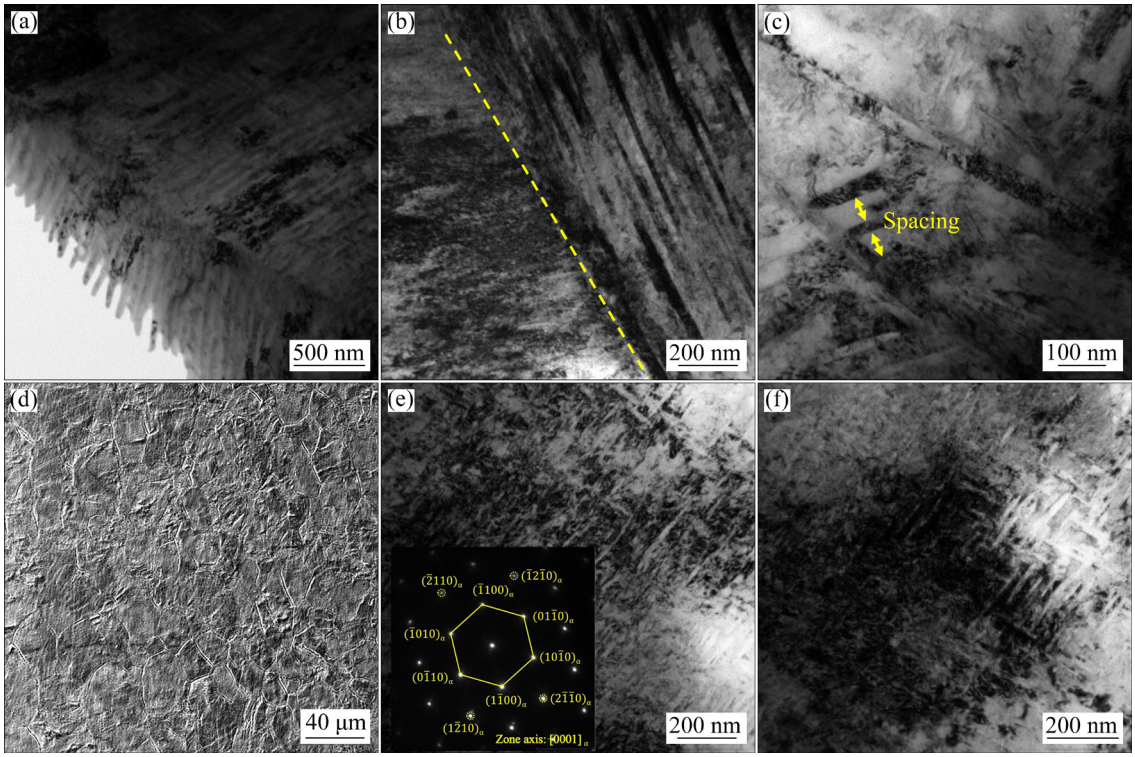

Fig. 5 TEM/SEM morphologies after Processes H (a−c) and I (d−f)

the phases *S*1 and *S*2. However, no silicide precipitates were found according to the TEM image (Fig. 5). This is mainly due to the low content of Si (only about one-tenth of the Si content in Refs. [19,20]) in this alloy. In this situation, all Si atoms can solute in α-Ti or β-Ti lattice.

3.2 Model building

By taking into account all the strengthening effects, the yield-strength model of the Ti−15Mo−2.7Nb−3Al−0.2Si alloy can be summarized in the following equation:

$$\sigma_{YS}=\sigma_0+\Delta\sigma_{ss}+\Delta\sigma_{gb}+\Delta\sigma_d+\Delta\sigma_p \quad (1)$$

where σ_0 means the intrinsic strength of a pure β-Ti without alloying elements. $\Delta\sigma_{ss}$, $\Delta\sigma_{gb}$, $\Delta\sigma_d$, and $\Delta\sigma_p$ indicate the strength increment contributed by the solid-solution-strengthening, grain-boundary-strengthening, dislocation-strengthening, and precipitation-strengthening, respectively.

As we know, a pure β-Ti does not exist at room temperature. Therefore, σ_0 cannot be obtained through experiments. It is widely accepted that the Peierls−Nabarro stress [21] can reflect the resistance of the lattice to dislocation motion. Therefore, in the present work, σ_0 was evaluated based on the calculated Peierls−Nabarro stress. According to Ref. [22], the Peierls−Nabarro stress (σ_{P-N}) can be expressed as

$$\sigma_{P-N}=\frac{2\mu}{1-\upsilon}\exp\left(\frac{-8\pi\zeta}{b}\right) \quad (2)$$

where μ is shear modulus, υ is Poisson's ratio, b is the magnitude of Burger's vector, and ζ is the half-width of the dislocation and can be expressed as Eq. (3):

$$\zeta=\frac{d}{2(1-\upsilon)} \quad (3)$$

where d indicates the interplanar spacing. For the pure α-Ti, d can be expressed as

$$d=1\Big/\sqrt{\frac{4}{3}\left(\frac{h^2+hk+k^2}{a^2}\right)+\left(\frac{l}{c}\right)^2}\ .$$

Based on previous research [23], the prismatic slip system of $\{10\bar{1}0\}\langle 11\bar{2}0\rangle$ can be activated most easily. Thus, a $\{10\bar{1}0\}\langle 11\bar{2}0\rangle$ slip system was used to calculate σ_{P-N} of pure α-Ti. Its corresponding b is $a/3\langle 11\bar{2}0\rangle$ with a magnitude of 0.295 nm [24−26]. The shear modulus, μ, and the Poisson's ratio, υ, are given as 42.65 GPa and 0.327, respectively [27]. By combining Eqs. (2) and (3), the calculated value of σ_{P-N} of pure α-Ti is 1.20×10^{-5} GPa.

For the pure β-Ti, d can be expressed as $a/\sqrt{h^2+k^2+l^2}$. It is known that the {110}⟨111⟩ slip system can be the most easily activated and therefore, was used to calculate σ_{P-N} of pure β-Ti. Its corresponding b is $a/2$⟨111⟩. The shear modulus, μ, and the Poisson's ratio, υ, are taken as 28.9 GPa and 0.33 (described above), respectively. By combining Eqs. (2) and (3), the calculated value of σ_{P-N} of pure β-Ti is 1.93×10^{-5} GPa. It can be easily found that the value of σ_{P-N} of pure β-Ti is approximately 1.6 times that of pure α-Ti. This trend indicates that the intrinsic strength of pure β-Ti (namely σ_0) could be approximately 1.6 times that of pure α-Ti. In Ref. [28], the intrinsic strength of pure α-Ti is considered as 250 MPa. Therefore, σ_0 in the present work can be calculated to be 401 MPa.

Ti−15Mo−2.7Nb−3Al−0.2Si alloy contains a high content of alloying elements. Thus, the solid-solution-strengthening effect, $\Delta\sigma_{ss}$, could be significant. According to GYPEN and DERUYTTERE [29] and TODA-CARABALLO et al [30], $\Delta\sigma_{ss}$ can be expressed as [31]

$$\Delta\sigma_{ss}=\left(\sum_i B_i^{3/2}X_i\right)^{2/3},\ B_i=M\mu\lambda_i^{4/3}Z \tag{4}$$

where B_i means the strengthening coefficient of the solute i, and X_i means the concentration of the solute i (at.%). M is the Taylor factor, and the value of 2.75 was adopted in the present work [32]. μ=28.9 GPa, Z is a fitting constant and was taken as 1.3×10^{-3} [33] in the present work. λ_i is the misfit parameter and can be expressed as

$$\lambda_i=\xi\left(\eta_i'^2+\theta^2\delta_i^2\right)^{1/2},\ \eta_i'=\frac{\eta_i}{1+0.5|\eta_i|} \tag{5}$$

where η_i means the shear-modulus misfit, and δ_i means the lattice-parameter misfit. They can be approximately expressed as

$$\eta_i=\frac{2(\mu_i-\mu_{Ti})}{\mu_i+\mu_{Ti}},\ \delta_i=\frac{2(\delta_i-\delta_{Ti})}{\delta_i+\delta_{Ti}}.$$

ξ equals 4 for body-centered-cubic (bcc) metals [30,31]. The value of θ depends on the dislocation types of the alloy during deformation [33]. According to Ref. [30], edge dislocation is the dominant dislocation type in face-centered-cubic (fcc) and bcc systems at room temperature, and thus θ was taken as 16 in the present work. Table 4 lists the parameters used for the calculation. By combining Eq. (4) and (5), the calculated value of $\Delta\sigma_{ss}$ is 205 MPa.

The grain-boundary-strengthening effect has been found by HALL [34] and PETCH [35] for approximately 70 years. It can be expressed as

$$\Delta\sigma_{gb}=k\frac{1}{\sqrt{D}} \tag{6}$$

where k is the grain-boundary-strengthening coefficient, and D is the grain size. The k values of many pure metals were listed in Ref. [36], including the hcp-Ti. However, the listed value cannot be used directly since Ti−15Mo−2.7Nb−3Al−0.2Si is an alloy and belongs to the bcc structure. In the present work, k was obtained through the linear fitting of the σ_{YS}–$D^{-1/2}$ relation after Processes SS, D, E, and F, as shown in Fig. 6. According to the slope of the fitting line, k equals 633 MPa·μm$^{1/2}$.

The preexisting dislocations in the alloy make it more difficult for dislocations to initiate and move and could lead to a significant increase in the yield strength. Therefore, the quantitative description of the dislocation-strengthening effect, namely $\Delta\sigma_d$, is very important for the precise adjustment of the yield strength. Equation (7) shows the classical forest-hardening model, which has been widely used [31,37,38]:

$$\Delta\sigma_d=M\alpha\mu b\rho^{1/2} \tag{7}$$

Table 4 Parameters of elements in Ti−15Mo−2.7Nb− 3Al− 0.2Si alloy

Element	μ/GPa	Atomic radius/nm	Atomic fraction/%	X_i	η_i	η_i'	δ_i	λ_i	B_i/MPa
Ti	45.6 [31]	0.145	47.87	0.8369	0	0	0	0	0
Mo	125.5 [31]	0.136	95.94	0.0810	0.934	0.637	−0.064	4.826	842.7
Nb	37.5 [31]	0.143	92.91	0.0152	−0.195	−0.178	−0.014	1.138	122.7
Al	26 [31]	0.143	26.98	0.0586	−0.547	−0.430	−0.014	1.935	249.2
Si	66.2 [31]	0.118	28.09	0.0038	0.369	0.311	−0.205	13.20	3222.9

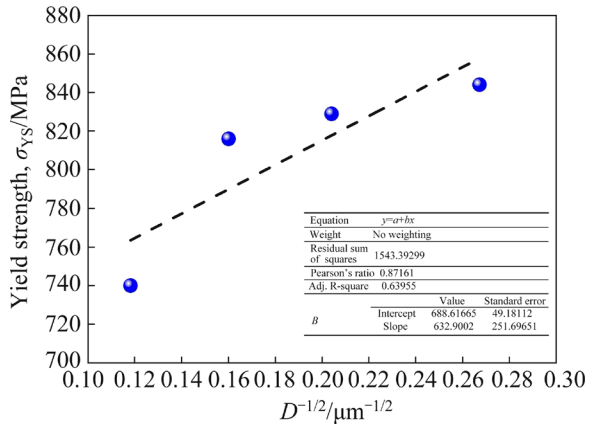

Fig. 6 σ_{YS}–$D^{-1/2}$ relation after Processes SS, D, E, and F

where ρ is the dislocation density. α is a dislocation-interaction constant, which takes 0.3 [31,37] in this study. $b=a/2\langle 111\rangle$ with a magnitude of 0.285 nm. ρ can be calculated by [39]

$$\rho=\frac{3E}{\mu b^2\left(1+2\upsilon^2\right)}\varepsilon^2 \tag{8}$$

where E means the elastic modulus, and ε means the microstrain.

Getting the value of ε is the key to calculating the dislocation-strengthening effect. The XRD profiles of the alloy under different conditions contain the information of ε. The Williamson−Hall equation [40−42] provides the solution to evaluate ε based on the XRD analysis, as shown in Eq. (9):

$$\beta_{hkl}\cos\theta_{hkl}=\frac{K\lambda}{D}+4\varepsilon\sin\theta_{hkl} \tag{9}$$

where θ_{hkl} means Bragg's angle, K is the shape factor and taken as 0.9, and λ means the wavelength of X-rays. β_{hkl} means the corrected instrumental broadening of the diffraction peak at $2\theta_{hkl}$, as shown in Eq. (10):

$$\beta_{hkl}=\sqrt{\beta^2_{hkl(\text{measured})}-\beta^2_{hkl(\text{instrumental})}} \tag{10}$$

$\beta_{hkl(\text{measured})}$ and $\beta_{hkl(\text{instrumental})}$ are characterized by the full width at half-maximum (FWHM) at $2\theta_{hkl}$. According to Eq. (9), it can be found that the corrected instrumental broadening is induced by two factors, namely the grain size, and microstrain. In the present work, D (tens of micrometers) is much larger than λ (several Å). Thus, the $K\lambda/D$ part in Eq. (9) is too small and could be neglected. Equation (9) can be rewritten as

$$\beta_{hkl}\cos\theta_{hkl}=4\varepsilon\sin\theta_{hkl} \tag{11}$$

Based on Eq. (11), ε can be obtained by drawing the $4\sin\theta_{hkl}$–$\beta_{hkl}\cos\theta_{hkl}$ relationship. The slope of the fitting line can be considered as ε. The $\beta_{hkl(\text{instrumental})}$ should be clarified. In the present work, the XRD profile after Process SS was used as the fundamental data to calculate the inherent instrumental-broadening effect of this equipment. In addition, $\beta_{hkl(\text{measured})}$ and $\beta_{hkl(\text{instrumental})}$ of different peaks were directly output, using the peak-fitting function (Gaussian fitting or Lorentz fitting) in the Origin software. Figures 7(a−c) show the comparisons of the XRD profiles of the Ti−15Mo−2.7Nb−3Al−0.2Si alloy among different processes. Figure 7(d) gives an example of the peak-fitting result after Process B (CR71%).

The authors tried to build the $4\sin\theta_{hkl}$–$\beta_{hkl}\cos\theta_{hkl}$ relationship through the linear fitting. However, the low-fitting precision makes it difficult to extract the valid ε values. Referring to Ref. [43], the authors decided to calculate ε directly at a selected θ_{hkl} according to $\varepsilon=(\beta_{hkl}\cos\theta_{hkl})/(4\sin\theta_{hkl})$ after each process. After the full consideration of the intensity and symmetry of different peaks, the decision was drawn that the peaks of $(110)_\beta$ were used for calculating ε after Processes A−F, and the peaks of $(211)_\beta$ were used after Processes G, H and I. Table 5 lists the calculated values of $\Delta\sigma_d$ after different processes. The parameters used for the calculation are also listed. It can be found that $\Delta\sigma_d$ ranges from 58 to 454 MPa in the present work. The recrystallization process after Processes D, E, and F can greatly reduce the dislocation density in the microstructure and lead to a great impairment of the dislocation-strengthening effect.

It is known that the existence of dislocations could lead to elastic lattice distortion. Therefore, by multiplying the microstrain, ε (listed in Table 5) and elastic modulus, E, of the Ti−15Mo−2.7Nb−3Al−0.2Si alloy (76.9 GPa), the residual stress (named as $\Delta\sigma'_d$) induced by dislocations can be calculated, namely $\Delta\sigma'_d=E\varepsilon$. To some extent, $\Delta\sigma'_d$ could also be considered as the strengthening effect of dislocations. The authors made a comparison between $\Delta\sigma'_d$ and the calculated $\Delta\sigma_d$ in Table 5, as shown in Fig. 8. It can be found that $\Delta\sigma'_d$ is higher than $\Delta\sigma_d$ and shows greater variance with increasing the dislocation density. This is possibly due to the fact that E is a macro parameter and is not proper to be used in the calculation of micro stress. The error

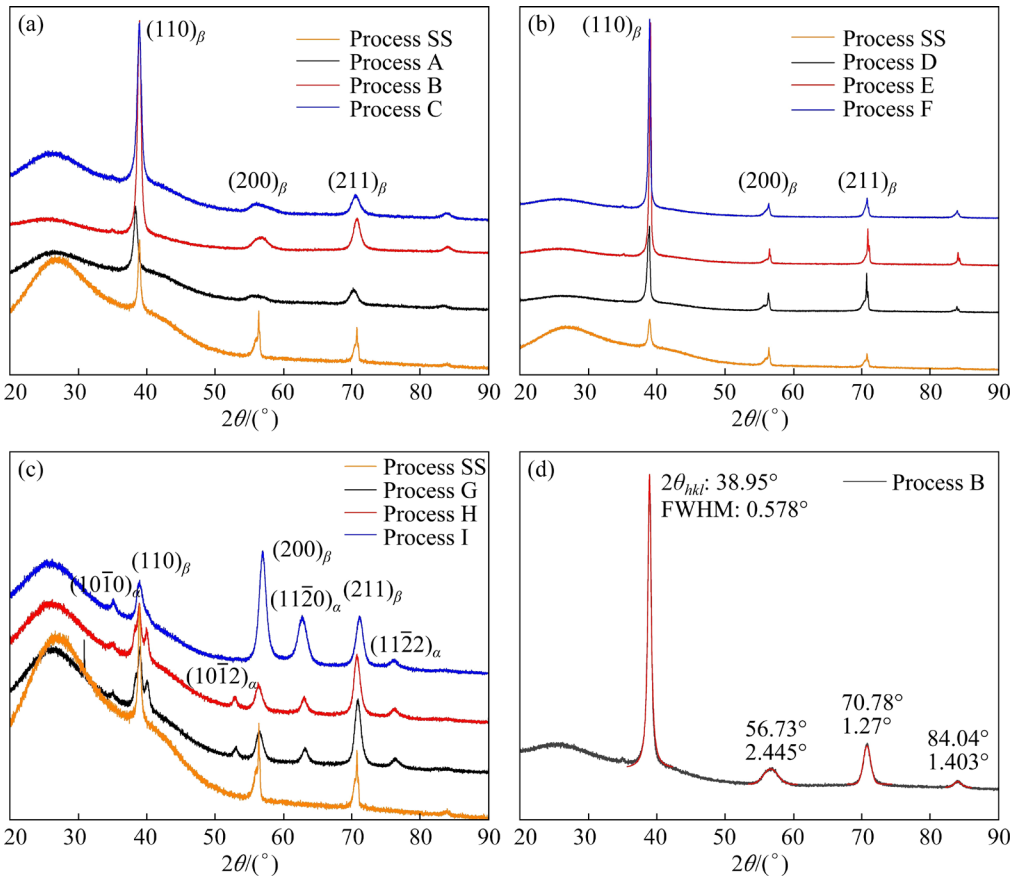

Fig. 7 Comparisons of XRD profiles of Ti−15Mo−2.7Nb−3Al−0.2Si alloy among different processes ((a) Processes SS, A, B and C; (b) Processes SS, D, E and F; (c) Processes SS, G, H and I) and example of peak-fitting result after Process B (d)

Table 5 Calculated values of dislocation-strengthening effect after different processes

Process	Peak position	β_{hkl}/rad	ε	ρ/m^{-2}	$\Delta\sigma_d$/MPa
A	$(110)_\beta$	8.61×10^{-3}	6.18×10^{-3}	3.08×10^{15}	377
B		6.84×10^{-3}	4.83×10^{-3}	1.88×10^{15}	295
C		9.60×10^{-3}	6.79×10^{-3}	3.72×10^{15}	414
D		1.35×10^{-3}	9.57×10^{-4}	7.39×10^{13}	58
E		–	–	–	–
F		–	–	–	–
G	$(211)_\beta$	1.80×10^{-2}	6.31×10^{-3}	3.21×10^{15}	385
H		1.79×10^{-2}	6.32×10^{-3}	3.22×10^{15}	386
I		2.13×10^{-2}	7.44×10^{-3}	4.47×10^{15}	454

could be magnified with increasing microstrain (namely dislocation density).

Precipitation-strengthening plays an important role in alloy strength. Two mechanisms (the cutting mechanism and the Orowan mechanism) are responsible for the precipitation-strengthening effect according to the penetrability of the precipitates to dislocations [44,45]. The Orowan mechanism was established based on the assumption that the precipitates are impenetrable to dislocations. The controlling mechanism of precipitation-strengthening is considered and therefore the most widely used [45]. In the present work, the Orowan-strengthening effect introduced by the needle-like

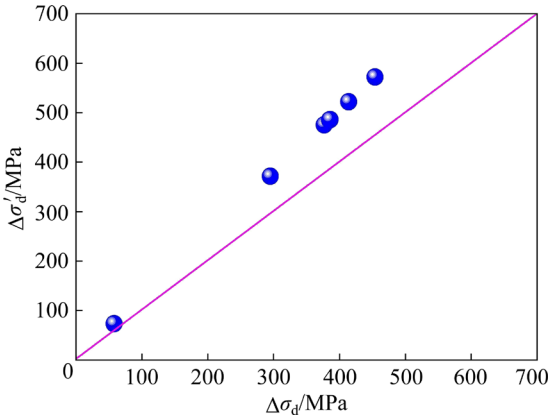

Fig. 8 Comparison between $\Delta\sigma_d'$ and $\Delta\sigma_d$

secondary α phase is given by [46]

$$\Delta\sigma_p = \frac{0.4M\mu b}{\pi\sqrt{1-\upsilon}}\frac{\ln(\bar{d}/b)}{\lambda_p} \quad (12)$$

where M=2.75, μ=28.9 GPa, b=0.285 nm, and υ=0.33. $\bar{d}$ indicates a mean diameter of random cross-sections of spherical precipitates. However, it should be noted that the needle-like precipitates in the present work have high aspect ratios and cannot be deemed as particles. To solve this problem, we take the mean thickness of the secondary α plates as $\bar{d}$. λ_p is the inter-precipitate distance.

Based on Fig. 5, the values of $\bar{d}$ and λ_p after Processes H and I were evaluated and are listed in Table 6. The precipitated secondary α phase after Process I has an average thickness of 14.9 nm and an average spacing of 39.3 nm, which are much smaller than the values after Process H. This trend follows the features shown in Fig. 5. According to Eq. (12), the Orowan-strengthening effect, $\Delta\sigma_p$, can be calculated. Due to the much thinner and denser secondary α phase after Process I, its $\Delta\sigma_p$ (355 MPa) is higher than that after Process H (284 MPa). According to Fig. 4, the precipitated secondary α phase after Processes G and H shows a similar size and distribution. Therefore, it is assumed that $\Delta\sigma_p$ after Process G is also 284 MPa.

Table 6 Evaluated Orowan-strengthening effect after Processes G−I

Process	$\bar{d}$ /nm	λ_p/nm	$\Delta\sigma_p$/MPa
G	–	–	284 (Referring to Process H)
H	49.5	64.0	284
I	14.9	39.3	355

3.3 Model verification

Based on the discussion of different strengthening effects, the specific yield-strength model of the Ti−15Mo−2.7Nb−3Al−0.2Si alloy can be summarized in the following equation:

$$\sigma_{YS} = 606 + \frac{653}{\sqrt{D}} + M\alpha\mu b\rho^{1/2} + \frac{0.4M\mu b}{\pi\sqrt{1-\upsilon}}\frac{\ln(\bar{d}/b)}{\lambda_p} \quad (13)$$

According to Eq. (13), the σ_{YS} values were calculated after different processes, as given in Table 7. To verify the prediction precision of the model, the calculated σ_{YS} values were compared with the experimental values, and the relative errors were computed. It can be found that Eq. (13) shows a good prediction performance. The absolute value of the prediction error ranges from 3% to 16.6%. In the present work, the dislocation-strengthening and precipitation-strengthening effects could mostly affect the yield strength of the Ti−15Mo−2.7Nb−3Al−0.2Si alloy.

3.4 Fractography

The fracture surfaces of alloys could reflect their mechanical properties. Figure 9 shows the typical fracture surfaces of the tensile specimens after Processes A, D, G, and I. It can be found that large dimples are distributed throughout the fibrous area after Processes A and D, which indicates good plasticity. After Process G (Figs. 9(c, d)), however, a portion of the intergranular fracture appears, and this trend corresponds to the loss of plasticity (or, in other words, the increase of strength). In particular, the intergranular fracture domains the fracture surface after Process I (Figs. 9(e, f)). This feature indicates that this alloy after Process I may obtain the lowest plasticity (or highest strength). The above results deduced from the fracture surfaces are consistent with the experiments.

Revealing the reason for the transition of the fracture mechanism from a dimpled fracture to an intergranular fracture is essential. In the authors' opinion, the precipitated secondary α phase is responsible for this phenomenon. The increasing volume fraction of the secondary α phase inside β grains could continuously strengthen the intragrain zone. This trend makes the grain boundaries become a relatively weak area. Therefore, an intergranular fracture appears and gradually dominates the fracture surface.

Table 7 Comparison between calculated and experimental values of yield strength after different processes

Process	σ_0/MPa	$\Delta\sigma_{ss}$/MPa	$\Delta\sigma_{gb}$/MPa	$\Delta\sigma_d$/MPa	$\Delta\sigma_p$/MPa	σ_{YS}(Cal.)/MPa	σ_{YS}(Exp.)/MPa	Error/%
SS	401	205	75	−	−	681	740	−8.0
A			75	377	−	1058	955	10.8
B			75	295	−	976	948	3.0
C			75	414	−	1095	939	16.6
D			101	58	−	765	816	−6.3
E			129	−	−	735	829	−11.3
F			169	−	−	775	844	−8.2
G			169	385	284	1444	1314	9.9
H			169	386	284	1445	1304	10.8
I			169	454	355	1584	1518	4.3

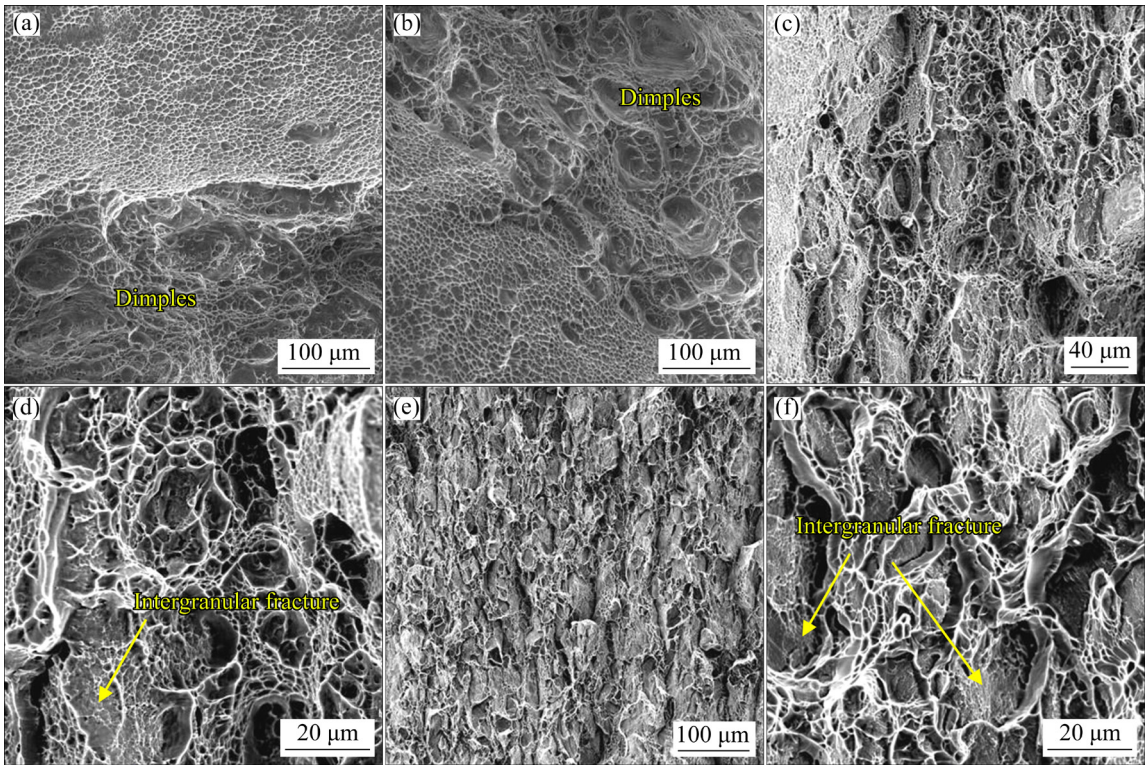

Fig. 9 Morphologies of fracture surfaces: (a) Process A; (b) Process D; (c, d) Process G; (e, f) Process I

4 Conclusions

(1) The highest yield strength of 1518 MPa was obtained after a combined process of cold rolling + recrystallization + cold rolling + duplex aging. This trend is mainly due to the much denser and thinner secondary α phase as well as the considerable density of remaining dislocations in the microstructure.

(2) Dislocation-strengthening and precipitation-strengthening effects could mostly affect the yield strength of this alloy. The established composite-strengthening model shows good prediction performance, for which the absolute value of the prediction error ranges from 3% to 16.6%.

(3) The increasing volume fraction of the secondary α phase could continuously strengthen the intragrain zone. This feature makes the grain boundaries become a relatively weak area. Therefore, an intergranular fracture appears and gradually dominates the fracture surface.

CRediT authorship contribution statement

Xiao-hui SHI: Project administration, Conceptualization, Writing − Original draft, Supervision; **Qi ZHANG:** Interpretation of data, Formal analysis, Writing − Review & editing; **Zhen JING, Zhi-yaun FAN:** Acquisition of data; **Jiang-lin LIU, Jun-wei QIAO:** Writing − Review & editing.

Declaration of competing interest

The authors declare that they have no known competing financial interests or personal relationships that could have appeared to influence the work reported in this paper.

Acknowledgments

The authors would like to acknowledge the financial support from the Fundamental Research Program of Shanxi Province, China (No. 202203021211130), and the National Natural Science Foundation of China (Nos. 51801132, 52075359). The authors would like to express their gratitude to Professor Peter K. LIAW for his help with grammar correction.

References

[1] SHANG Guo-qiang, ZHU Zhi-shou, CHANG Hui, WANG Xin-nan, KOU Hong-chao, LI Jin-shan. Development of ultra-high strength titanium alloy [J]. Chinese Journal of Rare Metals, 2011, 35: 286−291. (in Chinese)

[2] YU Fei-long, KONG C, YU Hai-liang. Low-temperature superplasticity of cryorolled Ti−6Al−4V titanium alloy sheets [J]. Tungsten, 2023, 5(4): 522−530.

[3] WU Yong, FAN Rong-lei, QIN Zhong-huan, CHEN Ming-he. Shape controlling and property optimization of TA32 titanium alloy thin-walled part prepared by hot forming [J]. Transactions of Nonferrous Metals Society of China, 2021, 31(8): 2336−2357.

[4] ZHANG Chang-jiang, JIANG Xi, LÜ Zhi-dan, FENG Hong, ZHANG Shu-zhi, XU Ying, HAYAT M D, CAO Peng. Effect of duplex aging on microstructure and mechanical properties of near-β titanium alloy processed by isothermal multidirectional forging [J]. Transactions of Nonferrous Metals Society of China, 2022, 32(4): 1159−1168.

[5] ZHANG Hao-yu, WANG Chuan, ZHOU Ge, ZHANG Si-qian, CHEN Li-jia. Dependence of strength and ductility on secondary α phase in a novel metastable-β titanium alloy [J]. Journal of Materials Research and Technology, 2022, 18: 5257−5266.

[6] LEE S W, OH J M, KIM J H, PARK C H, HONG J K, YEOM J T. Demonstration of martensite reorientation-induced plasticity by ultra-high strength titanium alloys [J]. Materials Science and Engineering A, 2021, 807: 140878.

[7] CHURCH N L, TALBOT C E P, WISE G J, SHAH O Y I, JONES N G. Development of ultra-high strength Ti−Nb−Sn alloys through grain-refinement by in situ Zener pinning [J]. Scripta Materialia, 2022, 218: 114809.

[8] CHEN Yi, LI Jin-shan, TANG Bin, KOU Hong-chao, XUE Xiang-yi, CUI Yu-wen. Texture evolution and dynamic recrystallization in a beta titanium alloy during hot-rolling process [J]. Journal of Alloys and Compounds, 2015, 618: 146−152.

[9] FERRERO J G. Candidate materials for high-strength fastener applications in both the aerospace and automotive industries [J]. Journal of Materials Engineering and Performance, 2005, 14: 691−696.

[10] MA Li-xia, WAN Min, LI Wei-dong, SHAO Jie, BAI Xue-piao. Constitutive modeling and processing map for hot deformation of Ti−15Mo−3Al−2.7Nb−0.2Si [J]. Journal of Alloys and Compounds, 2019, 808: 151759.

[11] XU T W, ZHANG S S, ZHANG F S, KOU H C, LI J S. Effect of ω-assisted precipitation on $\beta\rightarrow\alpha$ transformation and tensile properties of Ti−15Mo−2.7Nb−3Al−0.2Si alloy [J]. Materials Science and Engineering A, 2016, 654: 249−255.

[12] IVASISHIN O M, MARKOVSKY P E, MATVIYCHUK Y V, SEMIATIN S L, WARD C H, FOX S. A comparative study of the mechanical properties of high-strength β-titanium alloys [J]. Journal of Alloys and Compounds, 2008, 457: 296−309.

[13] XU T W, LI J S, ZHANG S S, ZHANG F S, LIU X H. Cold deformation behavior of the Ti−15Mo−3Al−2.7Nb−0.2Si alloy and its effect on α precipitation and tensile properties in aging treatment [J]. Journal of Alloys and Compounds, 2016, 682: 404−411.

[14] COURY F G, KAUFMAN M, CLARKE A J. Solid-solution strengthening in refractory high entropy alloys [J]. Acta Materialia, 2019, 175: 66−81.

[15] NAG S, BANERJEE R, SRINIVASAN R, HWANG J Y, HARPER M, FRASER H L. ω-assisted nucleation and growth of α precipitates in the Ti−5Al−5Mo−5V−3Cr−0.5Fe β titanium alloy [J]. Acta Materialia, 2009, 57: 2136−2147.

[16] GUO Shun, MENG Qing-kun, HU Liang, LIAO Guang-yue, ZHAO Xin-qing, XU Hui-bin. Suppression of isothermal ω phase by dislocation tangles and grain boundaries in metastable β-type titanium alloys [J]. Journal of Alloys and Compounds, 2013, 550: 35−38.

[17] CHEN Yang, FANG Qi-hong, LUO Si-hua, LIU Feng, LIU Bin, LIU Yong, HUANG Zai-wang, LIAW P K, LI Jia. Unraveling a novel precipitate enrichment dependent strengthening behaviour in nickel-based superalloy [J]. International Journal of Plasticity, 2022, 155: 103333.

[18] MANSOOR A, DU Wen-bo, YU Zi-jian, DING Ning, FU Jun-jian, LOU Feng, LIU Ke, LI Shu-bo. Effects of grain refinement and precipitate strengthening on mechanical properties of double-extruded Mg−12Gd−2Er−0.4Zr alloy [J]. Journal of Alloys and Compounds, 2022, 898: 162873.

[19] LUO X, LIU L H, YANG C, LU H Z, MA H W, WANG Z, LI D D, ZHANG L C, LI Y Y. Overcoming the strength-ductility trade-off by tailoring grain-boundary metastable Si-containing phase in β-type titanium alloy [J].

Journal of Materials Science & Technology, 2021, 68: 112−123.

[20] LUO X, YANG C, FU Z Q, LIU L H, LU H Z, MA H W, WANG Z, LI D D, ZHANG L C, LI Y Y. Achieving ultrahigh-strength in beta-type titanium alloy by controlling the melt pool mode in selective laser melting [J]. Materials Science and Engineering A, 2021, 823: 141731.

[21] HIRTH J P, LOTHE J. Theory of dislocations [M]. 2nd ed. New York: Wiley, 1982.

[22] NABARRO F R N. Fifty-year study of the Peierls−Nabarro stress [J]. Materials Science and Engineering A, 1997, 234/235/236: 67−76.

[23] WANG L, ZHENG Z, PHUKAN H, KENESEI P, PARK J S, LIND J, SUTER R M, BIELER T R. Direct measurement of critical resolved shear stress of prismatic and basal slip in polycrystalline Ti using high energy X-ray diffraction microscopy [J]. Acta Materialia, 2017, 132: 598−610.

[24] KO Y G, SHIN D H, PARK K T, LEE C S. An analysis of the strain hardening behavior of ultra-fine grain pure titanium [J]. Scripta Materialia, 2006, 54: 1785−1789.

[25] CONRAD H Effect of interstitial solutes on the strength and ductility of titanium [J]. Progress in Materials Science, 1981, 26: 123−403.

[26] DYAKONOV G S, ZEMTSOVA E, MIRONOV S, SEMENOVA I P, VALIEV R Z, SEMIATIN S L. An EBSD investigation of ultrafine-grain titanium for biomedical applications [J]. Materials Science and Engineering A, 2015, 648: 305−310.

[27] TROMANS D. Elastic anisotropy of Hcp metal crystals and polycrystals [J]. International Journal of Research & Reviews in Applied Sciences, 2011, 6: 462−483.

[28] CORDERO Z C, KNIGHT B E, SCHUH C A. Six decades of the Hall−Petch effect — A survey of grain-size strengthening studies on pure metals [J]. International Materials Reviews, 2016, 61: 495−512.

[29] GYPEN L A, DERUYTTERE A. Multi-component solid solution hardening [J]. Journal of Materials Science, 1977, 12: 1028−1033.

[30] TODA-CARABALLO I, RIVERA-DíAZ-DEL-CASTILLO P E J. Modelling solid solution hardening in high entropy alloys [J]. Acta Materialia, 2015, 85: 14−23.

[31] ZHAO G H, LIANG X Z, KIM B, RIVERA-DíAZ-DEL-CASTILLO P E J. Modelling strengthening mechanisms in beta-type Ti alloys [J]. Materials Science and Engineering A, 2019, 756: 156−160.

[32] ROSENBERG J M, PIEHLER H R. Calculation of the Taylor factor and lattice rotations for bcc metals deforming by pencil glide [J]. Metallurgical Transactions, 1971, 2: 257−259.

[33] ČIŽEK L, KRATOCHVÍL P, SMOLA B. Solid solution hardening of copper crystals [J]. Journal of Materials Science, 1974, 9: 1517−1520.

[34] HALL E O. The deformation and ageing of mild steel: III. Discussion of results [J]. Proceedings of the Physical Society, Section B, 1951, 64: 747−753.

[35] PETCH N. The cleavage strength of polycrystals [J]. J Iron Steel Inst Lond, 1953, 173: 25.

[36] WU D, ZHANG J Y, HUANG J C, BEI H, NIEH T G. Grain-boundary strengthening in nanocrystalline chromium and the Hall–Petch coefficient of body-centered cubic metals [J]. Scripta Materialia, 2013, 68: 118−121.

[37] ZHAO G H, XU X, DYE D, RIVERA-DíAZ-DEL-CASTILLO P E J. Microstructural evolution and strain-hardening in TWIP Ti alloys [J]. Acta Materialia, 2020, 183: 155−164.

[38] ZHAO Peng-cheng, YUAN Guang-jian, WANG Run-zi, GUAN Bo, JIA Yun-fei, ZHANG Xian-cheng, TU Shan-tung. Grain-refining and strengthening mechanisms of bulk ultrafine grained CP-Ti processed by L-ECAP and MDF [J]. Journal of Materials Science & Technology, 2021, 83: 196−207.

[39] CHRISTIEN F, TELLING M T F, KNIGHT K S. Neutron diffraction in situ monitoring of the dislocation density during martensitic transformation in a stainless steel [J]. Scripta Materialia, 2013, 68: 506−509.

[40] MOTE V D, PURUSHOTHAM Y, DOLE B N. Williamson−Hall analysis in estimation of lattice strain in nanometer-sized ZnO particles [J]. Journal of Theoretical and Applied Physics, 2012, 6: 6.

[41] PRABHU Y T, RAO K V, KUMAR V, KUMARI B S. X-ray analysis by Williamson−Hall and size-strain plot methods of ZnO nanoparticles with fuel variation [J]. World Journal of Nano Science & Engineering, 2014, 4: 21−28.

[42] ALY K A, KHALIL N M, ALGAMAL Y, SALEEM Q M A. Estimation of lattice strain for zirconia nano-particles based on Williamson-Hall analysis [J]. Materials Chemistry and Physics, 2017, 193: 182−188.

[43] BUSHROA A R, RAHBARI R G, MASJUKI H H, MUHAMAD M R. Approximation of crystallite size and microstrain via XRD line broadening analysis in TiSiN thin films [J]. Vacuum, 2012, 86: 1107−1112.

[44] MOON J, KIM S, JANG J I, LEE J, LEE C. Orowan strengthening effect on the nanoindentation hardness of the ferrite matrix in microalloyed steels [J]. Materials Science and Engineering A, 2008, 487: 552−557.

[45] MEYERS M A, CHAWLA K K. Mechanical behavior of materials [M]. Prentice Hall, New Jersey, 1999.

[46] MA K K, WEN H M, HU T, TOPPING T D, ISHEIM D, SEIDMAN D N, LAVERNIA E J, SCHOENUNG J M. Mechanical behavior and strengthening mechanisms in ultrafine grain precipitation-strengthened aluminum alloy [J]. Acta Materialia, 2014, 62: 141−155.

超高强 Ti−15Mo−2.7Nb−3Al−0.2Si 钛合金的强化行为及模型

石晓辉[1]，张 琪[1]，荆 镇[1]，范智渊[1]，刘江林[2]，乔珺威[1]

1. 太原理工大学 材料科学与工程学院，太原 030024；
2. 太原理工大学 机械与运载工程学院，太原 030024

摘 要：基于 XRD、OM、SEM 和 TEM 分析，研究超高强 Ti−15Mo−2.7Nb−3Al−0.2Si 钛合金的组织演变及强化行为。结果表明，位错强化和析出强化效应对该合金的屈服强度影响较大。冷轧+再结晶+冷轧+双时效组合工艺可获得 1518 MPa 的最高屈服强度，这主要归因于显微组织中的高密度残存位错及密集而细小的次生 α 相。建立复合强化模型，其预测误差在 16.6%以内。此外，研究发现次生 α 相体积分数的增加可以不断强化晶内区域，这使得沿晶断裂开始出现并逐渐占据整个断裂面。

关键词：强化模型；超高强；强化行为；钛合金；Ti−15Mo−2.7Nb−3Al−0.2Si

(Edited by Bing YANG)